ARTICLE

Alleviating Structure Collapse of Polycrystalline LiNi$_x$Co$_y$Mn$_{1−x−y}$O$_2$ via Surface Co Enrichment

Mingjie Shang,[∥] Hengyu Ren,[∥] Wenguang Zhao, Zijian Li, Jianjun Fang, Hui Chen, Wenguang Fan,* Feng Pan,* and Qinghe Zhao*

Read Online

ACCESS | Metrics & More | Article Recommendations | SI Supporting Information

ABSTRACT: The structure collapse issues have long restricted the application of polycrystalline LiNi$_x$Co$_y$Mn$_{1−x−y}$O$_2$ (NCM) at high voltages beyond 4.4 V vs Li/Li$^+$. Herein, for LiNi$_{0.55}$Co$_{0.12}$Mn$_{0.33}$O$_2$ (P-NCM), rapid surface degradation is observed upon the first charge, along with serious particle fragmentation upon repeated cycles. To alleviate these issues, a surface Co enrichment strategy is proposed [i.e., Co-enriched NCM (C-NCM)], which promotes the in situ formation of a robust surface rock-salt (RS) layer upon charge, serving as a highly stable interface for effective Li$^+$ migration. Benefiting from this stabilized surface RS layer, Li$^+$ extraction occurs mainly through this surface RS layer, rather than along the grain boundaries (GBs), thus reducing the risk of GBs' cracking and even particle fragmentation upon cycles. Besides, O loss and TM (TM = Ni, Co, and Mn) dissolution are also effectively reduced with fewer side reactions. The C-NCM/graphite cell presents a highly reversible capacity of 205.1 mA h g$^{−1}$ at 0.2 C and a high capacity retention of 86% after 500 cycles at 1 C (1 C = 200 mA g$^{−1}$), which is among the best reported cell performances. This work provides a different path for alleviating particle fragmentation of NCM cathodes.

KEYWORDS: LiNi$_x$Co$_y$Mn$_{1−x−y}$O$_2$, structure collapse, rock-salt layer, grain-boundary, particle fragmentation
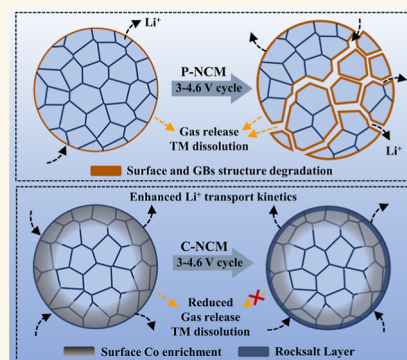
With the rapid development of clean energy technologies in modern society, electrified equipment such as portable electronic devices and electric vehicles is gradually becoming more popular in daily life. Thus, lithium-ion batteries (LIBs), an important part of electrification, are required for higher energy density, longer service life, and a lower price. Seeking high-performance cathode materials has been considered one of the biggest bottlenecks that restricts the popular application of LIBs. Among multiple cathodes, Ni-rich ternary layered oxide (LiNi$_x$Co$_y$Mn$_{1−x−y}$O$_2$, abbreviated as NCM) stands out as the most promising one due to its high energy density and low cost characteristics.

However, when operated at high voltages (>4.4 V vs Li$^+$/Li), the application of NCM materials faces severe surface degradation issues, i.e., the surface rock-salt (RS) phase formation induced by lattice O loss. The surface NiO-type RS phase with a high impedance can significantly deteriorate the Li$^+$ diffusion kinetics and decrease the practical capacity. Meanwhile, O$_2$ released from NCM materials can further cause the oxidation and decomposition of electrolyte components, such as ethylene carbonate (EC) and ethyl methylcarbonate (EMC), leading to an unstable cathode electrolyte interface (CEI). Thus, the vulnerable surface of pristine NCM materials

has been regarded as the structure origin for deteriorating their cycle stability and then hindering their practical applications.[1−3]

Besides the vulnerable surface, the polycrystalline feature of NCM cathodes makes them tend to crack along grain boundaries (GBs), which is induced by the anisotropic stress accumulation.[4] Generally, the formation of intragranular cracks can be directly associated with the high voltage cycle,[5] and the state-of-charge (SOC) heterogeneity caused by the different Li$^+$ diffusion kinetics results in internal stress accumulation. After the cyclic charge/discharge process, the heterogeneity of delithiated degrees among the primary particles leads to uneven intragranular stress.[6,7] The heterogeneity of adjacent particles determines that, for each primary particle, the stress density on the surface is greater than that in the core.[8] That is
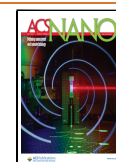
to say, in the secondary particles, stress mainly accumulates along GBs, which is consistent with the phenomenon that secondary particles always crack along GBs. Besides, the randomly arranged orientation of primary particles inside a secondary particle prolongs the Li$^+$ diffusion path, generating anisotropic stress between the primary particles and thus inducing cracks along GBs.[9,10] These cracks are particularly hazardous because the electrolyte can permeate into the interior of NCM particles along these microcracks, which leads to severe interface side reactions, triggers the irreversible phase change, and then causes the corresponding capacity decay.[11]

As discussed above, resolving the issues of surface degradation and GBs' cracking is very important for the development of advanced NCM cathode materials. Tremendous efforts have been made to stabilize the structure of Ni-rich cathode materials,[12] including element doping,[13−15] surface coating,[16−18] electrolyte modification,[19−21] GBs enhancement,[22,23] etc. However, obtaining stable cycling of the NCM-layered cathode at high voltages (>4.4 V) remains very challenging, and most of the previous works improved the stability of NCM via sacrificing the capacity.

Reviewing all the optimizations above, we find it necessary to investigate the important role of Co element, and the optimization effects can be listed as follows: (1) enhance thermal stability and stabilize the layered structure at high temperature by reducing the Li/O loss,[24,25] (2) suppress the Li$^+$/Ni^{2+} disorder and enhance the Ni^{2+} stability, which can reduce the irreversible phase change upon cycle,[26−29] (3) optimize electrode properties such as electronic/ionic conductivity and rate performance, and (4) provide additional capacity by the redox of Co^{3+}/Co^{4+}.[27,30] Thus, Co can provide preferable electrode properties, as well as structure stability, in NCM cathodes. However, the method and mechanism of Co utilization to enhance the structure stability of NCM cathodes still remain vague.

Herein, we take LiNi$_{0.5}$Co$_{0.2}$Mn$_{0.3}$O$_2$ (P-NCM) as a model, and the surface Co-enriched NCM (C-NCM) is synthesized to alleviate the structure collapse issues of NCM cathodes. In particular, the Co-enriched surface can induce the in situ formation of a robust RS layer on the surface of C-NCM upon the first cycle. Benefited from both the Co-rich surface region and the reinforced surface RS layer, the stabilized surface structure and enhanced Li$^+$ diffusion kinetics are obtained with homogeneous Li$^+$ extraction from the bulk of C-NCM, thus reducing the risk of GBs' cracking and even particle fragmentation upon cycle. Consequently, C-NCM exhibits excellent cell performance with high capacity and long-term cycling stability, i.e., the C-NCM/graphite cell presents a highly reversible capacity of 205.1 mA h g^{-1} at 0.2 C and a high capacity retention of 86% after 500 cycles at 1 C.

RESULTS AND DISCUSSION

Surface Co Enrichment. In this work, to achieve surface Co enrichment, a multistep synthesis is performed, including solution treatment, manual mixing, high-temperature sintering, etc. Specifically, the commercial Ni$_{0.55}$Co$_{0.12}$Mn$_{0.33}$(OH)$_2$ precursors are first uniformly coated with different contents of Co(OH)$_2$ via coprecipitation reaction; then, the coated precursors are manually ground and mixed with LiOH·H$_2$O powder with the stoichiometric Li/TM ratio of 1.03 (TM represents the sum of Co, Ni, and Mn), and finally, all the obtained mixtures are sintered at 900 °C for 12 h in an air atmosphere to obtain the surface Co-enriched NCM (Figures

1a and S1). Four kinds of surface Co-enriched products are designed and synthesized, with mass ratios of cobalt of
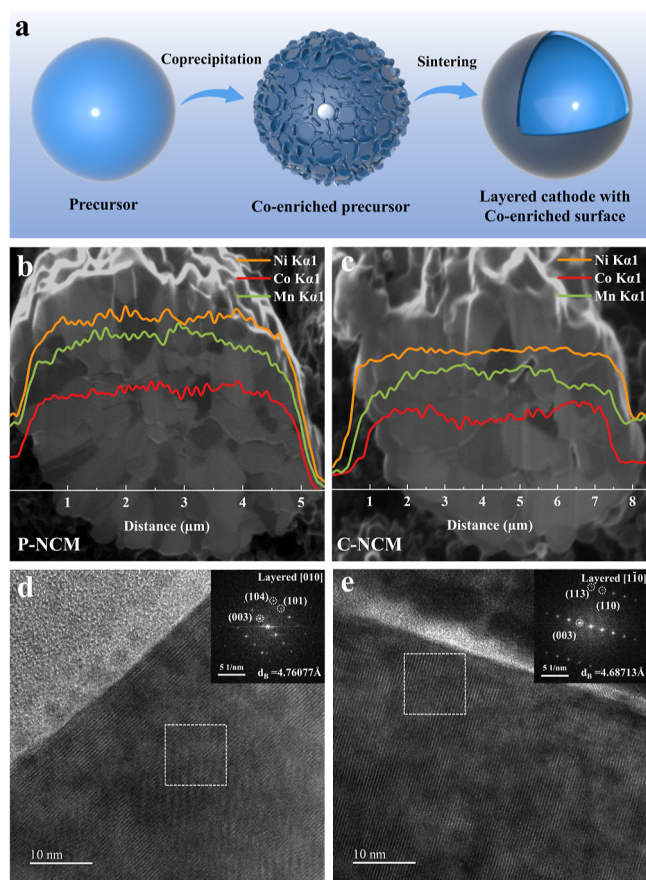

Figure 1. Schematic diagrams for (a) material preparation. The cross-sectional morphology and element distributions of (b) P-NCM and (c) C-NCM. The surface structures and the correlated diffraction patterns of (d) P-NCM and (e) C-NCM, as obtained via TEM characterizations.

approximately 2.5, 5, 10, and 15%, and the obtained products are labeled C-1, C-2, C-3, and C-4, respectively. Table S1 shows the chemical formulas of the obtained products based on experimental design and inductively coupled plasma mass spectrometry tests, showing the high consistency between the designed and obtained products. Figure S2 shows the morphology of the products. All the products present a similar polycrystalline feature with a primary particle size of about 200−300 nm and a secondary particle size of 5−6 μm. By comparing the cell performance of NCM/Li cells at 25 and 45 °C (Figure S3), it is realized that the cycle stability gradually enhances as the surface Co enrichment increases. To reveal the mechanism of surface Co enrichment, we select C-3 as the subject of research, which is labeled as the C-NCM, and pristine LiNi$_{0.55}$Co$_{0.12}$Mn$_{0.33}$O$_2$ (P-NCM) is selected for comparison.

The cross-sectional morphologies of P-NCM and C-NCM are shown in Figure 1b,c. Although the products show similar polycrystalline features, the element distributions are obviously different. For P-NCM, Ni, Co, and Mn are uniformly distributed across the overall particle, while for C-NCM, obvious Co enrichment is observed in the surface region of the particle. We further notice that the surface Co enrichment reaches a high thickness of up to 2 μm, which can significantly
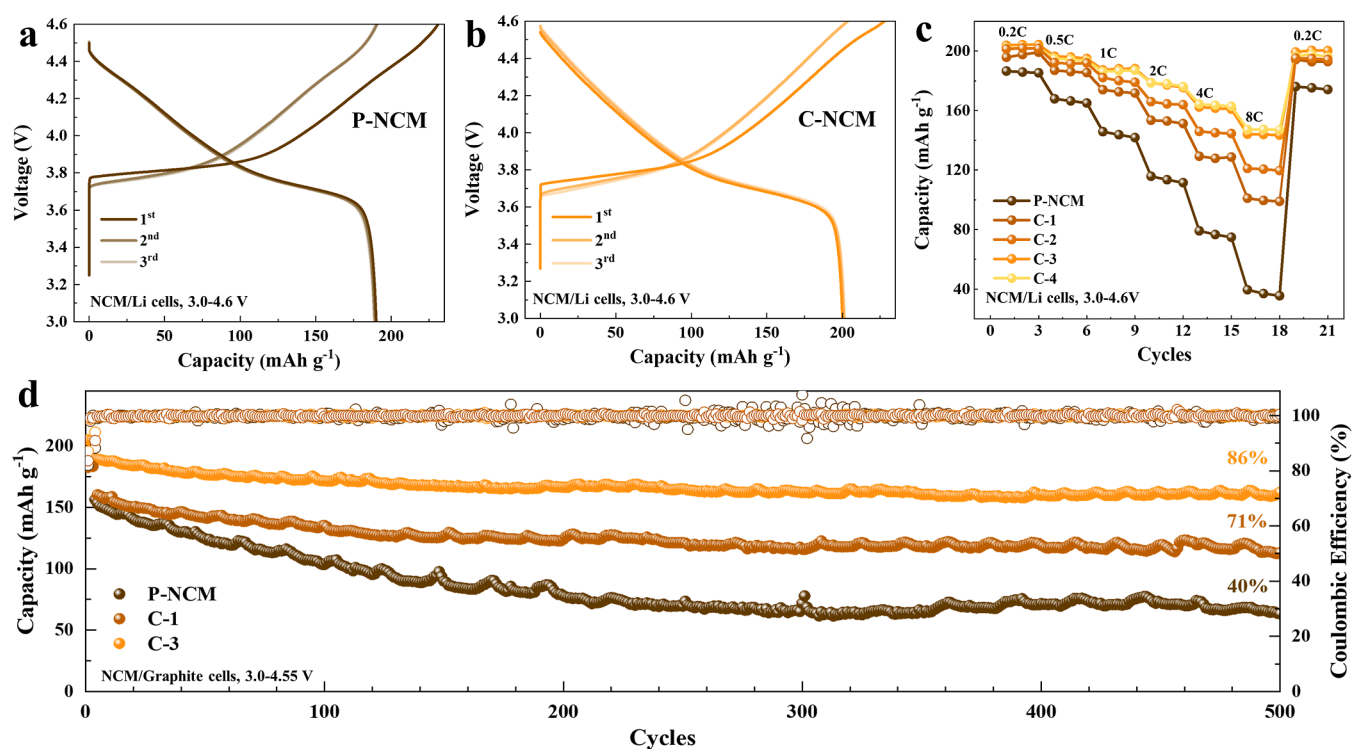
Figure 2. Charge/discharge curves of (a) P-NCM/Li and (b) C-NCM/Li cells in the initial three cycles, with a current of 0.2 C (1 C = 200 mA g^{-1}) and a potential range of 3−4.6 V. The comparison of (c) rate performances between P-NCM, C-1, C-2, C-3 (C-NCM), and C-4 in NCM/Li cells, with a potential range of 3−4.6 V. The comparison of (d) cycle performances between P-NCM, C-1, and C-3 (C-NCM) in NCM/graphite cells, with a current of 1 C and a potential range of 3−4.55 V.

affect the physicochemical properties of C-NCM.[31,32] Figure 1d,e shows the surface structures and the correlated diffraction patterns of the two products, as obtained via transmission electron microscopy (TEM) characterizations. The results show that both the surface structures of two products present a layered structure, and the surface Co enrichment causes a slight decrease in the surface layer spacing from 4.76 to 4.69 Å. Besides, the layered structures of products are further confirmed by the X-ray diffraction (XRD) refinements, as shown in Figure S4 and Table S2. The influence of surface Co enrichment on the physicochemical properties of C-NCM is further analyzed by the powder conductivity test (Figure S5).[33] The results indicate that as the surface Co enrichment increases, the powder conductivity gradually declines. When the Co enrichment reaches 15%, i.e., the C-4 product, it presents an ultra-low powder conductivity, which is very close to that of the pure LiCoO$_2$. That is to say, for the C-4 product, the surface of particles is nearly the same as that of pure LiCoO$_2$, which further emphasizes the existence of surface Co enrichment. Therefore, in this section, we propose the surface Co enrichment on C-NCM, which is beneficial for regulating the interface reactions from the material aspect and thus enhancing the electrode performances of the polycrystalline NCM cathode.

Cell Performance. Surface Co enrichment can cause improvements in both cycle stability and rate performances, which are comprehensively tested using both the NCM/Li cells (coin-type cells in the lab) and the NCM/graphite cells. Figure 2a,b shows the charge/discharge curves of P-NCM/Li and C-NCM/Li cells in initial 3 cycles, with a current of 0.2 C (1 C = 200 mA g^{-1}) and in a potential range of 3−4.6 V. For P-NCM, the initial Coulombic efficiency (ICE) is 82.3%, and

the discharge capacities are 190.02, 189.16, and 188.72 mA h g^{-1} in the first, second, and third cycles, respectively. For C-NCM, the ICE is 87.8%, and the discharge capacities are 200.0, 201.0, and 201.5 mA h g^{-1} in the first, second, and third cycles, respectively. The increase in ICE values with increased surface Co enrichment can further be confirmed by the results in Figure S6. Figures 2c and S7 show the comparison of rate performances. The rate performance is greatly promoted as the surface Co enrichment increases from 0% (P-NCM) to 15% (C-4). A huge promotion in rate performance can be further reflected in the rate capacities at a current of 8 C, i.e., the discharge capacity of C-NCM at a current of 8 C is 144.1 mA h g^{-1}, which is about 3.7 times higher than that of P-NCM (39.5 mA h g^{-1}). The above results illustrate that surface Co enrichment can effectively improve both the ICE and discharge capacity, which is closely related to the regulated interface reactions and reduced polarization and will be discussed in the following part.

We further performed the cycle stability tests with NCM/Li cells at 3−4.6 V (Figure S3) and NCM/graphite full cells at 3−4.55 V (Figures 2d and S8). The above tests exhibit the same trend of cycle stability, that is, the cycle stability of the NCM cathode increases with the increase of surface Co enrichment. Specially, the C-NCM/graphite cell presents a high discharge capacity of 189.73 mA h g^{-1} at a current of 1 C and a high retention of 86% after 500 cycles, which is among the best reported NCM cathodes (Table S3). The correlated charge/discharge curves of every 100 cycles are presented and compared in Figure S9. Besides, the environmental sensitivity of NCM cathodes has long been a challenge for industry.[34] To confirm the enhanced environmental stability, these products are further treated in two kinds of ways, including being placed
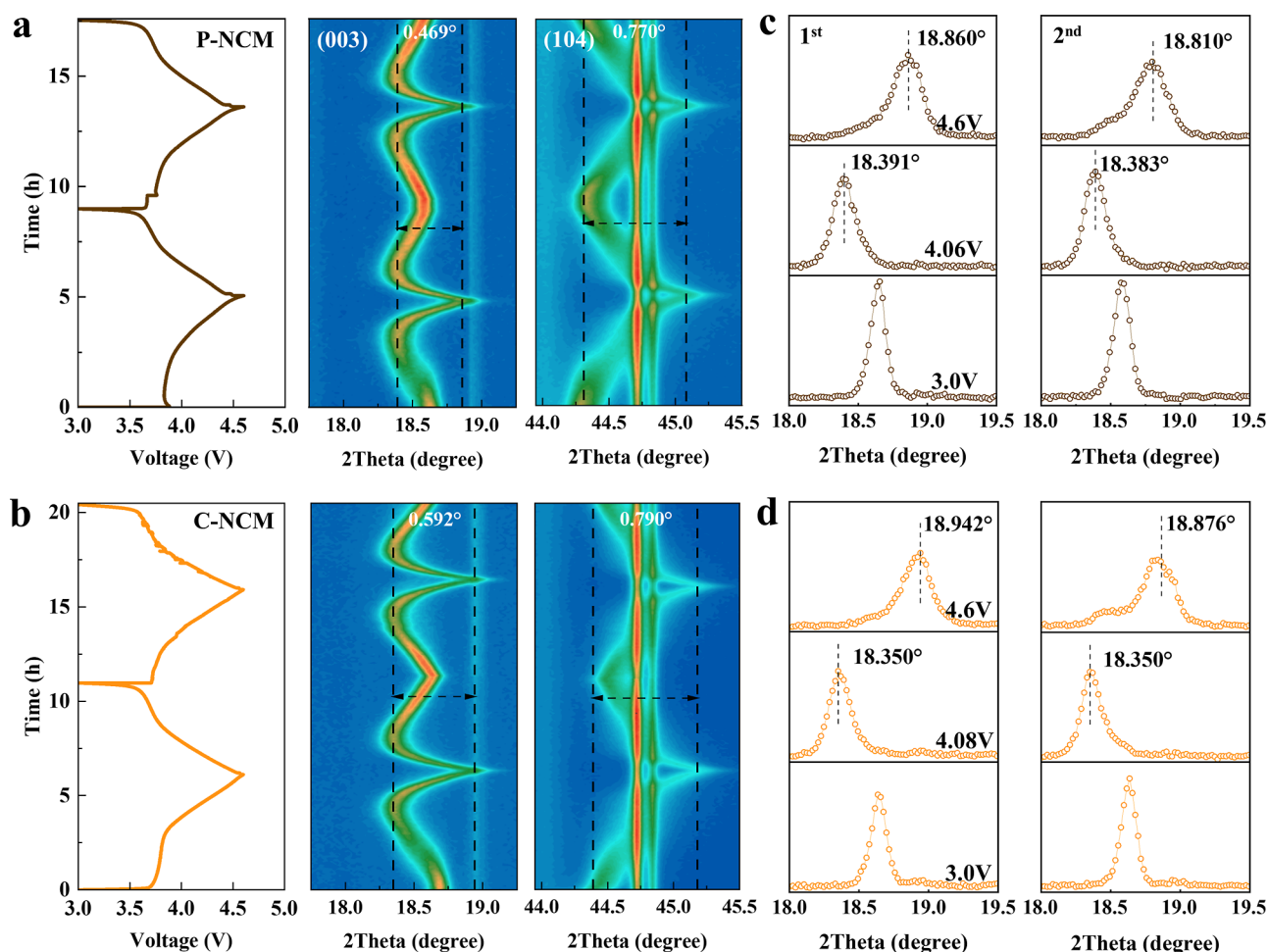
Figure 3. In situ XRD measurements of (a) P-NCM and (b) C-NCM in NCM/Li cells at 0.2 C with a potential range of 3−4.6 V. The leftmost (at about 4.1 V) and rightmost (at about 4.6 V) peaks of (003) planes for the initial 2 cycles of (c) P-NCM and (d) C-NCM.

in air (with a dew point temperature of 20.8 °C, in Shenzhen, China) for 7 days and in water for 12 h, respectively. The obtained products are then dried at 150 °C in air to remove the absorbed surface H_2O, and then the corresponding electrodes are manufactured and tested in NCM/Li cells (Figure S10). The results indicate that both the cycle stability and discharge capacity of the C-NCM/Li cell are obviously superior to those of the P-NCM/Li cell, demonstrating an obviously enhanced environment stability due to the surface Co enrichment. In summary, surface Co enrichment causes great promotion in cycle stability, rate performance, and environment stability of NCM cathodes.

Phase Transition Behavior. The phase transition behavior is a significant influence factor for the cell performances of NCM cathodes.[3,12] To probe the phase transition behavior, we perform in situ XRD of the NCM/Li cells in a potential range of 3−4.6 V and at a low current of 0.2 C, as shown in Figure 3a,b. The results show the similar peak variations of two cathodes for both the (003) and (104) planes, which are located at peak values of 18.6 and 44.3° (2theta, 2θ), respectively. Upon charge, for both cathodes, the layer spacing of (003) and (104) planes first increases (left shift of peaks) gradually until charge reaches 4.1 V and then decreases (right shift of peaks) gradually until charge reaches 4.6 V. The amplitude of changes in the lattice parameters of NCM cathodes can be indirectly acknowledged via comparing

the range of changes in the layer peak positions ($\Delta 2\theta$).[35,36] We observe that, upon charging to 4.6 V, the $\Delta 2\theta$ values of P-NCM and C-NCM cathodes are 0.469 and 0.592° for the variation of (003) peaks and 0.770 and 0.790° for the variation of (104) peaks, respectively. That is to say, the peak variations of C-NCM are obviously higher than those of P-NCM, showing the larger changes in lattice parameters. According to the results in Figure 2a,b, it is acknowledged that the C-NCM can deliver about 10% more capacity than P-NCM, i.e., causing more Li$^+$ removal from the cathode, thus leading to higher lattice parameter variation.

Upon more subtle analyses, the leftmost (at about 4.1 V) and rightmost (at about 4.6 V) peaks of the (003) planes of the two cathodes are further presented in Figure 3c,d. For P-NCM, such as in the second cycle, the leftmost and rightmost peaks of (003) planes are located at 2θ of 18.383 and 18.810°, and for C-NCM, they are located at 2θ of 18.350 and 18.876°, respectively, which further confirm the higher lattice parameter variations of the C-NCM cathode. Generally, the performance of a polycrystalline NCM cathode can be influenced by multiple factors, including surface regulation, bulk structure stability, the bonding strength of GBs, etc.[37] For the bulk structure stability, the higher the lattice parameter variation, the poorer the cycle stability.[38,39] In this work, compared with P-NCM, despite the higher lattice variations, the C-NCM achieves superior cycle stability, which is indeed an abnormal
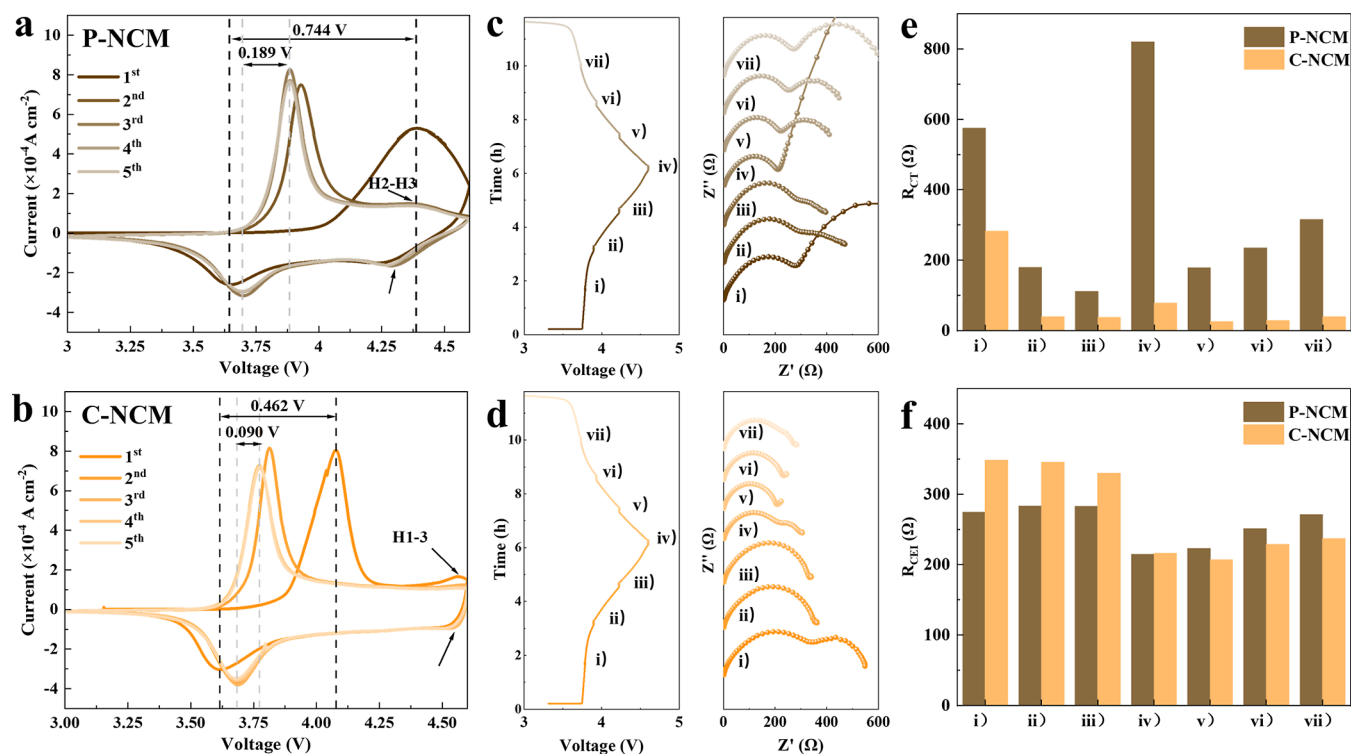
Figure 4. CV curves of (a) P-NCM and (b) C-NCM in NCM/Li cells in initial 5 cycles, with a scan rate of 0.2 mV s^{-1} and a potential range of 3−4.6 V. The in situ EIS measurements of (c) P-NCM and (d) C-NCM in NCM/Li cells in the 1st cycle (the EIS results are stacked along the Y-axis), and the corresponding fitting results of (e) R_{CT} and (f) R_{CEI}.
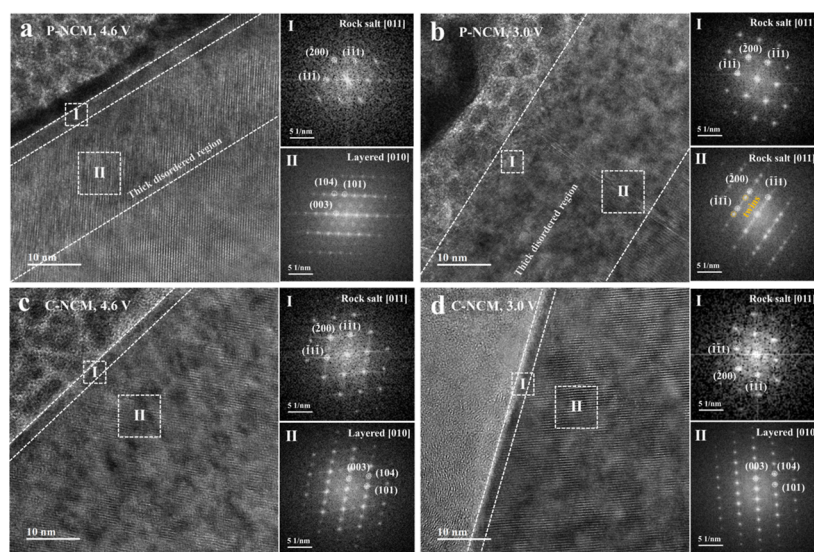

Figure 5. Surface structures of P-NCM upon a (a) fully charged state, 4.6 V, and (b) fully discharged state, 3.0 V, and the surface structures of C-NCM upon a (c) fully charged state, 4.6 V, and (d) fully discharged state, 3.0 V, both in the 1st cycle in NCM/Li cells.

phenomenon, and the surface Co enrichment is regarded as the origin for this abnormal result. We speculate that surface Co enrichment plays vital roles in regulating surface reactions and optimizing the Li$^+$ transport behaviors, thus alleviating the capacity decay issues from both the surface deterioration and the GBs' cracking-induced particle fragmentation, which will be discussed subsequently.

Regulated Surface Reaction Kinetics. To probe the regulated surface reactions, a comparison of cyclic voltammetry (CV) curves and electrochemical impedance spectroscopy (EIS) plots of NCM/Li cells is performed. Both the CV and

EIS are sensitive to detecting electrode interface reactions.[40−44] Figure 4a,b shows the CV curves of NCM/Li cells in the initial 5 cycles and potential range of 3−4.6 V, with a scan rate of 0.2 mV s^{-1}. For both cells, the CV curves in the first cycle are very different from those of the following cycles, mainly due to the surface phase transition in the first cycle.[45] This phase transition occurs from layer to RS, as illustrated in the following part. After 3 cycles, the CV curves of both cells are stabilized, indicating the stabilized surface. We find that there exist two main differences between the CV curves of two cells. First, for the redox peaks around 3.6−3.9 V, the
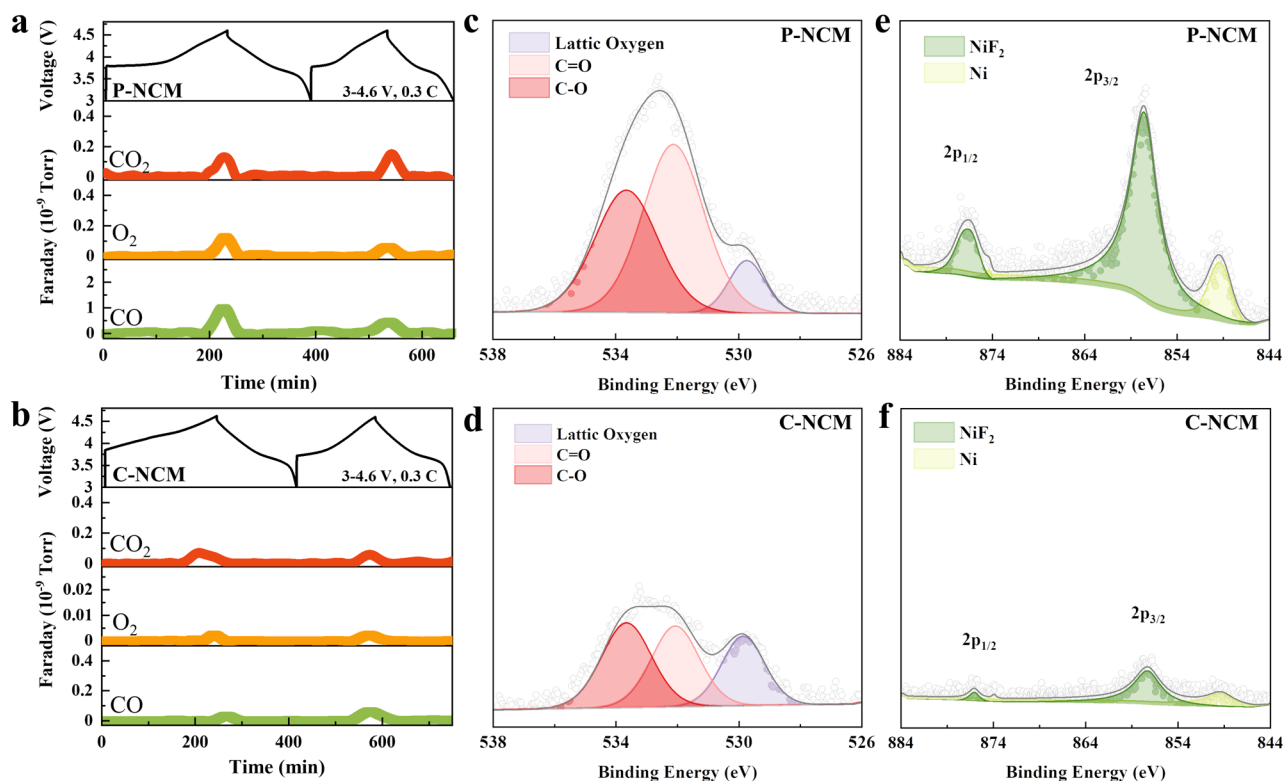
Figure 6. In situ DEMS measurements of (a) P-NCM and (b) C-NCM, both at 0.3 C with a potential range of 3−4.6 V. The XPS spectra results of NCM cathodes for O 1s of (c) P-NCM and (d) C-NCM. The XPS spectra results of Li metal anodes for Ni 2p of (e) P-NCM and (f) C-NCM.

separations of the redox peak positions of the P-NCM/Li and C-NCM/Li cells are 0.189 and 0.090 V, respectively, illustrating the reduced redox polarization. Second, the configuration of the CV curves of two cells in the potential range of 4.2−4.6 V is also very different, indicating the different high-voltage reactions. We observe that the CV curves in 4.2−4.6 V are very similar to those of the $LiCoO_2$/Li cells,[35] as shown in Figure S11, which further highlights the role of surface Co enrichment in regulating surface reactions.

The in situ EIS in the first cycle is performed to reveal the electron/Li^+ transport impedance through the interface of cathodes, as shown in Figure 4c,d. The EIS plots contain two impedance semicircles and one diffusion tail, which correspond to the impedance of CEI (R_{CEI}), the charge transfer impedance across the surface phase transition layer (PTL) (R_{CT}), as well as further Li^+ ion diffusion inside the bulk lattice structure, respectively.[40,46,47] The CEI is covered on the outermost surface of the cathode and originates from the interface reactions between the cathode and electrolyte.[48,49] The PTL is the transformed TM−O frameworks in the surface region, which refers in particular to the RS phase in this work.[50] Figure 4e,f shows the corresponding fitting results of the in situ EIS plots. The results indicate that the two cells show relatively similar values of R_{CEI} but very different values of R_{CT}, in which the C-NCM shows much smaller values of R_{CT} than P-NCM. Thus, the above results indicate that the main difference between two kinds of cathodes focuses on the properties of surface PTL rather than the properties of CEI, and surface Co enrichment can greatly optimize the electron/Li^+ transport behavior across the surface PTL. The enhanced Li^+ transport kinetics can further be characterized by the galvanostatic intermittent titration technique (GITT), and the calculation of

the diffusion kinetics (D_{Li^+}) is presented in Figure S12. During the overall charge/discharge process, the values of D_{Li^+} of C-NCM are obviously higher than those of P-NCM, further confirming the beneficial roles of surface Co enrichment on promoting the Li^+ transport kinetics.

Stabilized Surface Structure. The above discussions indicate that the relatively superior cell performance of C-NCM mainly originated from the optimized surface structure rather than the bulk. Thus, TEM characterizations are applied to reveal this optimized surface structure. Figure 5 shows the surface structures of P-NCM and N-NCM upon the fully charged and fully discharged states in the first cycle (in NCM/Li cells), respectively. For P-NCM, once charged to 4.6 V (Figure 5a), a pronounced transition from layered to nonlayered phases is observed in the surface region, with a thin outermost surface RS layer and a relatively thick subsurface disordered region, with thicknesses of 3 and 20 nm, respectively. Despite the fact that the thick subsurface disordered region still maintains a layered structure, a very strong glide of TM−O layers is detected, leading to the large lattice internal stress, which is regarded as the origin of the thick PTL in the surface of P-NCM.[11] Upon discharging to 3.0 V (Figure 5b), we find that the surface RS layer and the thick subsurface disordered region are well retained. Notably, the diffraction pattern of the subsurface thick disordered region inhibits two sets of diffraction spots, indexing to the layered phase and RS phase, respectively. The results indicate that the phase transition from layered to RS phase occurs not only in the outermost surface region but also in the subsurface region of P-NCM.

Figure 5c,d shows the surface structures of C-NCM at fully charged and fully discharged states, respectively. Similar to P-
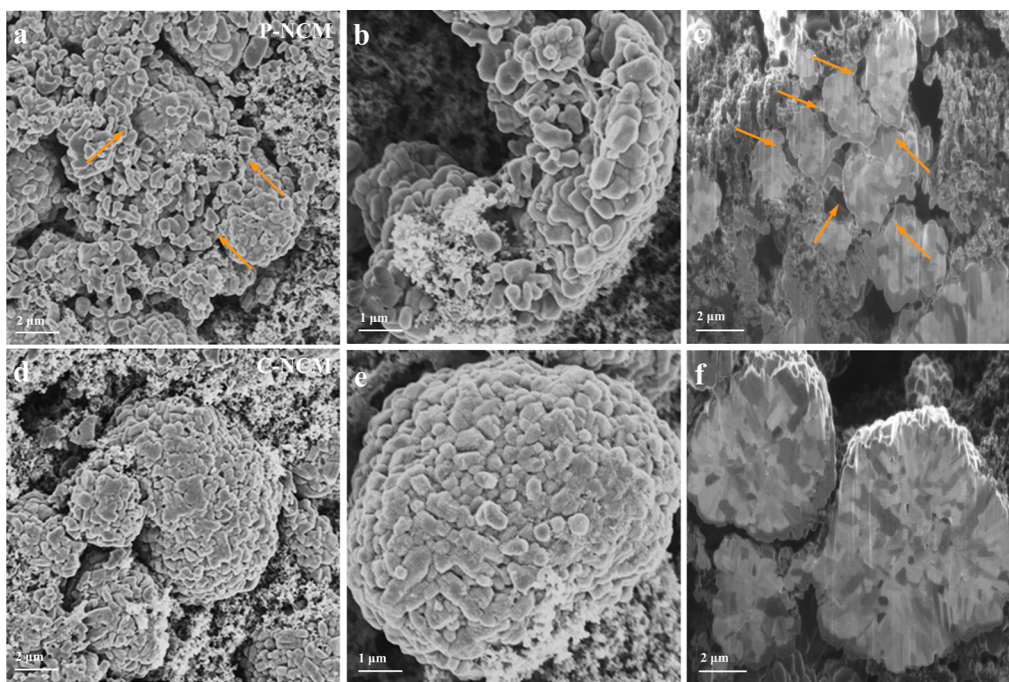
Figure 7. SEM morphology of (a,b) P-NCM cathodes in NCM/Li cells with a potential range of 3−4.6 V after 50 cycles at the current of 1 C and (c) its cross-sectional morphology. The SEM morphology of (d,e) C-NCM cathodes in NCM/Li cells with a potential range of 3−4.6 V after 50 cycles at a current of 1 C and (f) its cross-sectional morphology.

NCM, a thin surface RS layer is clearly in situ formed in the outermost surface region of C-NCM. However, the subsurface region of C-NCM presents totally different features. Whether it is at fully charged or fully discharged states, the subsurface region of C-NCM always shows a pure layered structure, and no signals of TM−O layer gliding are detected, illustrating the superior structure stability and enabling the superior Li$^+$ transport across the surface region of C-NCM. Since the most significant difference between the surface structures lies in the difference of Co enrichment, it can be concluded that the Co-enriched surface of C-NCM has a higher durability to maintain its original layered structure than that of P-NCM. A possible explanation may be as follows: the Ni in the TM−O layer is more likely to migrate toward the Li−O layer and causes the formation of Li/Ni antisites to promote the formation of nonlayer phases,[51,52] which hardly occurs for the Co in the TM−O layer, especially in the Co-enriched TM−O layer. The layered structure feature of the Co-enriched subsurface of C-NCM can be well retained even after 50 cycles (Figure S13b), further confirming the stabilization effect of surface Co enrichment. As a comparison, for the subsurface region of P-NCM, it has totally transformed to the RS phases (Figure S13a). This thick subsurface RS phase layer existing on P-NCM after cycles is completely different from the RS layer induced by the Co-enriched layer on C-NCM. The former one mainly consists of disordered NiO, and this disordered NiO RS phase presents unfavorable Li ion diffusion kinetics and high R_{CT} upon cycles (Figure S14). However, the dense RS layer induced by the Co-enriched layer exhibits much better structural stability and more promoted Li ion diffusion kinetics (Figure S14).

Generally, the surface phase transition of NCM cathodes from the layered phase to the RS phase is accompanied by the occurrence of the O loss from the Li−TM−O lattice. There are two pathways for the gas release: one is the unstable cathode surface structure upon high voltage, which leads to the O$_2$ release, and another is the oxidation of the electrolyte, which leads to CO$_2$ and CO gas release.[53,54] The detection of the above gases is performed via differential electrochemical mass spectrometry (DEMS), and the in situ DEMS spectra in the initial 2 cycles are presented in Figure 6a,b. The results indicate that the release of all gases for C-NCM is much lower than that of P-NCM. The lesser release of CO$_2$ and CO is mainly due to the lesser surface oxidation reaction of carbonate electrolytes, and the lesser O$_2$ release indicates the lesser O loss from the Li−TM−O lattice in the surface region. It is highlighted that, in this study, the NCM cathodes are synthesized without coating any inert elements, such as Al, F, P, etc.; therefore, upon charging, the highly oxidative Ni^{4+}/Co^{4+} and O^{n-} ($0 < n < 2$) ions in the NCM surface are directly contacted with the electrolyte and inevitably lead to the formation of the surface RS layer. However, these in situ-formed surface RS layers present different blocking effects on the O loss, i.e., the Co-enriched RS layer inhibits a higher blocking effect on O loss than the Ni-enriched RS layer, thus helping maintain the subsurface layered structure of the C-NCM.

The blocking effect of the Co-enriched RS layer on O loss can be further identified by the X-ray photoelectron spectroscopy (XPS) results. Figures S15 and 6c,d show the C 1s and O 1s XPS spectra results of electrodes after 50 cycles. The C 1s peaks can be separated into six peaks, including carbon black, C−O or CH$_2$−CF$_2$, O−C−O or C═O, O−C═O, Li$_2$CO$_3$ or CF$_2$, and CF$_3$, located at binding energies of 284.6, 286.2, 287.6, 288.9, 290.8, and 293.3 eV, respectively. The O 1s peaks can be separated into three peaks, including lattice oxygen, C═O, and C−O, locating at binding energies of 529.1, 532.0, and 533.8 eV, respectively.[55] Furthermore, the relative contents of each peak are calculated and shown in Table S4. We define the organic components in the CEI as the sum of
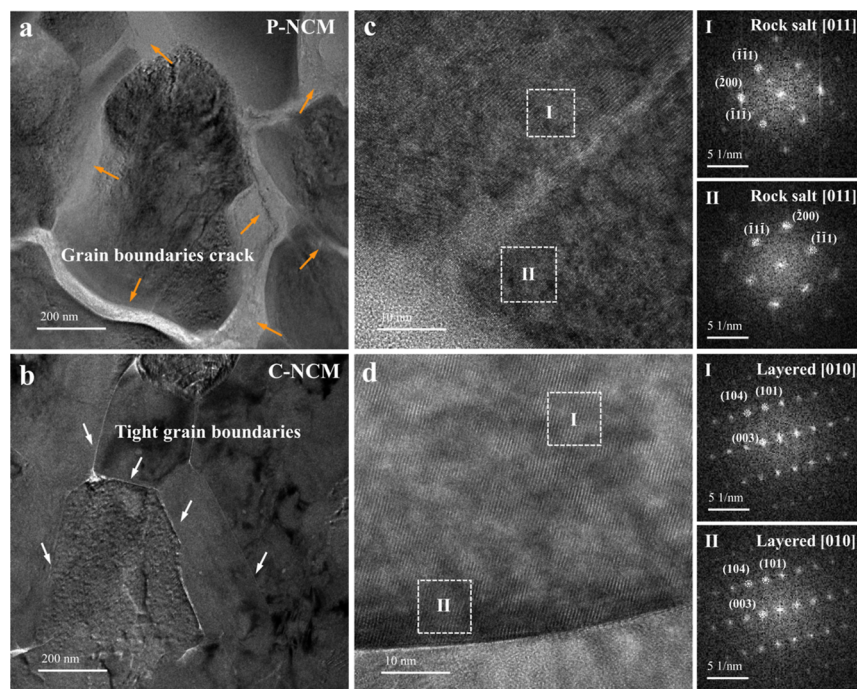
Figure 8. Structures in the GBs region of (a) P-NCM and (b) C-NCM via TEM characterizations in NCM/Li cells with a potential range of 3−4.6 V after 50 cycles at the current of 1 C and the corresponding GBs crack region of (c) P-NCM and tight GBs region of (d) C-NCM.
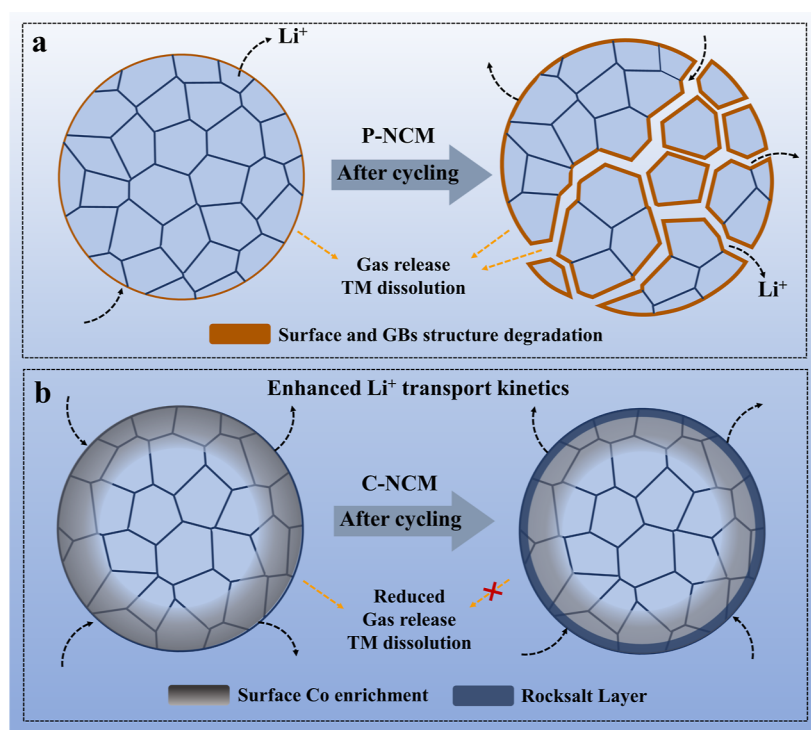

Figure 9. Schematic diagrams for (a) fragmentation of P-NCM and (b) reduced particle fragmentation of C-NCM.

O−C−O, C=O and O−C=O products, and the comparison results indicate that the organic ratio in CEI of P-NCM is obviously higher than that of C-NCM, further confirming the reduced solvent's decomposition on the surface of C-NCM. Due to the reduced side reactions, the TM dissolution is also effectively inhibited. Taking the Ni element as a sample, in Figure 6e,f, after 50 cycles, the signals of both the Ni and NiF$_2$ components on the Li metal anodes obtained from the C-

NCM/Li cell are obviously lower than those from the P-NCM/Li cell, demonstrating the obviously suppressed TM dissolution due to the Co-enriched surface RS layer. Thus, combining the above results, we confirm the formation of a thin and compact Co-enriched RS layer on the surface of C-NCM, which plays significant role in reducing both the O loss and TM dissolution issues.

Reduced Particle Fragmentation. Accompanied by the optimized surface structure, for C-NCM, the occurrence of GBs cracking is also greatly inhibited upon cycles. Figure 7a,d shows the scanning electron microscopy (SEM) morphology results of the NCM cathodes after 50 cycles at a current of 1 C. The results indicate that, for P-NCM, the polycrystalline particles have been in a fragmented state, and this particle fragmentation mainly originated from the cracks' generation and expansion along the GBs. In contrast, for C-NCM, the particles preserve their pristine spherical features, without any particle fragmentation. This reduced particle fragmentation can be further confirmed by the cross-sectional morphology, as shown in Figure 7e,f. For P-NCM, the particles have fragmented into several parts, while for C-NCM, no GBs cracking is observed across the overall particles. Therefore, surface Co enrichment can not only optimize the surface structure but also inhibit the occurrence of GBs cracking, leading to enhanced cycle stability. Figure 8 compares structures in the GBs regions of two NCM cathodes after 50 cycles upon a subtler observation. An obvious cracking of GBs is observed among the primary particles of P-NCM, as shown in Figure 8a. Analyzing the crystal structure near the GBs cracking, an obvious RS layer is observed on the surface of the primary particle (Figure 8b), indicating a higher SOC nearby the GBs region. In contrast, for C-NCM, no GBs cracking is observed among the primary particles, and the layered structure on the surface of the primary particle nearby the GBs is well preserved (Figure 8c,d).

As reported previously, the particle fragmentation of polycrystalline NCM usually originates from the GBs cracking.[4,8] Once the GB cracking appears on the surface, the electrolyte will penetrate into the interior of the particles along the generated cracks, which can promote the cracks' expansion and ultimately lead to particle fragmentation. The occurrence of GBs cracking is closely related to the inhomogeneity of Li$^+$ extraction from the surface of NCM particles.[6,7] If the Li$^+$ extraction across the particles is in a very homogeneous state, then the risk of GB cracking can be greatly reduced. Therefore, we consider that in this work, one of the most important roles of surface Co enrichment is to enhance the Li$^+$ extraction homogeneity from the C-NCM cathode. As compared in Figure 5, the most significant difference between the P-NCM and C-NCM cathodes lies in the different surface structures formed in the first cycle. For P-NCM, a thick surface PTL layer forms rapidly in the first cycle with a large R_{CT} value, while for C-NCM, a thin and uniform surface RS layer forms with a much smaller R_{CT} value. It can be easily acknowledged that the optimized surface of C-NCM can enable facile and homogeneous Li$^+$ extraction across the surface. Therefore, compared with the P-NCM, the Li$^+$ extraction through the surface region of GBs for C-NCM can be greatly restrained, resulting in smaller internal stress and a much closer SOC in the region of GBs, thus reducing the GBs cracking and then the following particle fragmentation.

Figure 9 presents the schematic diagrams for the reduced particle fragmentation of C-NCM. For the P-NCM with uniformly distributed Co elements across the overall particles, the surface structure rapidly deteriorates upon cycles, leading to more Li$^+$ extraction through GBs, causing GBs to crack and the following particle fragmentation. As a comparison, for C-NCM with surface Co enrichment, a thin and tough surface RS layer can be rapidly formed, acting as a facile Li$^+$ extraction pathway, which not only enables the Li$^+$ extraction

homogeneity but also reduces Li$^+$ extraction through GBs near the surface, thus resulting in the reduced GBs cracking as well as the reduced particle fragmentation. As the particle fragmentation reduces, the conductive network between the C-NCM particles and conductive agents is preserved well upon cycles, thus guaranteeing the excellent cycle stability of C-NCM.

CONCLUSIONS

In summary, this work provides a different surface Co enrichment strategy, which can effectively alleviate the structural collapse of LiNi$_x$Co$_y$Mn$_{1-x-y}$O$_2$ (NCM), including both surface degradation and particle fragmentation issues. The benefiting effects originated from the following aspects, i.e., first, the surface Co enrichment promotes the in situ-formed surface RS layer, which serves as a highly stable interface for cyclic Li$^+$ migration; second, the tough surface RS layer not only reduces the side reactions via suppressing the O loss and TM dissolution but also inhibits the particle fragmentation via reducing the Li$^+$ extraction from GBs' region. Thus, the surface Co-enriched NCM (C-NCM) achieves obviously enhanced cycle stability, rate performances, as well as enhanced environment stability. This work provides a different insight into achieving advanced polycrystalline cathodes.

EXPERIMENTAL SECTION

Sample Preparation. In this work, 10 g of the commercial precursor (XP55C, purchased from Zhejiang Haichuang Lithium Battery Technology Co., Ltd.) and corresponding stoichiometric amounts of CoSO$_4$ (mass ratios of Co are 2.5, 5, 10, and 15%) were dissolved in 30 mL of deionized water; we used LiOH as a precipitant and stirred at 60 °C for 4 h to make sure Co was enriched on the surface of the precursor via a coprecipitation method. The surface-modified precursor was collected and dried at 80 °C for 8 h. Then, the coated precursors are manually ground and mixed with LiOH·H$_2$O powder with a stoichiometric Li/TM ratio of 1.03 (TM represents the sum of Co, Ni, and Mn). After 900 °C sintering for 12 h in an air atmosphere, a series of NCM cathode materials with a Co-enriched surface (denoted as Table S1) are obtained.

Material Characterization. Morphology and elemental distribution investigations of the samples were conducted using a scanning electron microscope (Zeiss SUPRA-55) with an X-Max EDS detector. All XRD and in situ XRD measurements were performed on a Bruker D8 Advance diffractometer using a Cu Kα radiation source at 40 kV and 80 mA. Rietveld refinements of XRD patterns were carried out using the FULLPROF suite. The TEM images were collected on field-emission transmission electron microscopy (FETEM, JEOL-3200FS) operating at an accelerating voltage of 300 kV with a 60 cm camera length, a minimum collection angle of −30 to 30°, and a OneView CMOS camera (Gatan Inc.). TEM samples were prepared using a focused ion beam (FIB). The cross-sectional sample of the individual particle was attained by FIB as well. The chemical states of the selected elements were investigated by XPS on a Thermo Scientific Escalab 250Xi spectrometer. Powder conductivity was tested by a two-probe method (IEST-PRCD3100). Operando DEMS measurements were performed on a custom-built DEMS device. The DEMS cells were initially left to stand for 1 h, and galvanostatic charging was performed using a NEWARE electrochemical workstation. The resistivity is measured on a sample disc (0.15 g sample per disc under 5 MPa) by the four-point probe resistance tester. The dynamic pressure conductivity of samples was measured by Kelvin four-wire combining dual-disk electrode resistance measurement (IEST, PRCD1100).

Electrochemical Characterization. The cathode material was prepared by mixing active material, conductive acetylene black, and

polyvinylidene difluoride (PVDF) binder at a mass ratio of 8:1:1. The slurry was then cast on Al foil and dried in a vacuum oven overnight. The active material loading of the cathodes is approximately 1.5 mg/cm². The electrochemical performance was carried out by coin-type (CR2032) NCM/graphite full cells. The anode material was prepared by mixing graphite together with acetylene black and PVDF in a mass ratio of 8:1:1 as well. The slurry was coated on Cu foil and dried in a vacuum oven, and a process of prelithiation for 30 min was performed before being used as an anode. NCM/graphite cells were assembled in an argon-filled glovebox using the Celgard 2400 polypropylene membrane as the separator and 1.0 M $LiPF_6$ dissolved in a mixture of ethyl carbonate/ethyl methyl carbonate/fluoroethylene carbonate (EC/EMC/FEC) as the electrolyte, provided by Guangdong Canrd New Energy Technology Co., Ltd. and Guangzhou Tianci High-Tech Materials Co., Ltd., respectively. NCM/Li cells were also assembled under the same circumstances, in which Li metal foil was used as an anode instead. The charge/discharge performance was carried out in the NEWARE battery test system (provided by Shenzhen NEWARE Technology Ltd.). To analyze the long-term cyclability, the coin cells were charged and discharged at 0.2 C (1 C = 200 mA g^{-1}) for 3 cycles and then at 1 C for a long cycle. Rate performance was carried out at 0.2, 0.5, 1, 2, 4, 8, and 0.2 C, each for 3 cycles in NCM/Li cells between 3 and 4.6 V. The electrochemical tests of NCM/graphite cells were carried out at room temperature (25 °C) between 3 and 4.55 V, while NCM/Li cells were tested between 3 and 4.6 V. All tests were performed after an 8 h rest. The GITT measurement was obtained by the NEWARE system, and the relaxation time was set to 30 min after each current pulse for 10 min. The CV test and EIS were performed on a Solartron Analylical 1470E electrochemical workstation. The CV test was carried out with a scan rate of 0.2 mV s^{-1} and a potential range of 3−4.6 V. The frequency range of the EIS test was 1000 kHz to 0.01 Hz.

ASSOCIATED CONTENT

ⓢ Supporting Information

The Supporting Information is available free of charge at https://pubs.acs.org/doi/10.1021/acsnano.4c03128.

> Characterizations of materials such as SEM, XRD, FIB, TEM, and XPS; electrochemical characterizations such as cycle and rate performance, GITT, CV test, and EIS; SEM morphology of pristine and $Co(OH)_2$-coated $Ni_{0.55}Co_{0.12}Mn_{0.33}(OH)_2$ precursor; measured and designed chemical formulas of products; SEM morphology of pristine and surface C-NCM materials; cycle stability of the NCM/Li cells of different samples; XRD patterns of the products of different samples; fitted lattice parameters of P-NCM and C-NCM; powder conductivity of different samples and pure LCO; ICE of different samples; comparison of charge/discharge curves at various rate currents; comparison of electrochemical performance between our work and other reports; comparison of the charge/discharge curves of every 100 cycles; comparison of the environment stability; CV curves of LCO/Li cell; comparison of GITT curves and correlated calculation results of diffusion kinetics; comparison of surface structures, XPS results of C 1s spectra and corresponding relative contents after 50 cycles; and comparison of EIS plots and fitted results (PDF)

AUTHOR INFORMATION

Corresponding Authors

Wenguang Fan − *School of Advanced Materials, Peking University Shenzhen Graduate School, Shenzhen 518055, China*; Email: fanwg@pku.edu.cn

Feng Pan − *School of Advanced Materials, Peking University Shenzhen Graduate School, Shenzhen 518055, China;* ⓞ orcid.org/0000-0002-8216-1339; Email: panfeng@pkusz.edu.cn

Qinghe Zhao − *School of Advanced Materials, Peking University Shenzhen Graduate School, Shenzhen 518055, China*; Email: zhaoqh@pku.edu.cn

Authors

Mingjie Shang − *School of Advanced Materials, Peking University Shenzhen Graduate School, Shenzhen 518055, China*

Hengyu Ren − *School of Advanced Materials, Peking University Shenzhen Graduate School, Shenzhen 518055, China*

Wenguang Zhao − *School of Advanced Materials, Peking University Shenzhen Graduate School, Shenzhen 518055, China*

Zijian Li − *School of Advanced Materials, Peking University Shenzhen Graduate School, Shenzhen 518055, China*

Jianjun Fang − *School of Advanced Materials, Peking University Shenzhen Graduate School, Shenzhen 518055, China; Qiantu Battery Technology Co., Ltd, Dongguan 523808, China*

Hui Chen − *School of Materials and Environmental Engineering, Shenzhen Polytechnic University, Shenzhen 518055, China*

Complete contact information is available at:
https://pubs.acs.org/10.1021/acsnano.4c03128

Author Contributions

‖M.S. and H.R. contributed equally to this work.

Notes

The authors declare no competing financial interest.

ABBREVIATIONS

RS, rock-salt; GBs, grain boundaries; LIBs, lithium ion batteries; NCM, $LiNi_xCo_yMn_{1−x−y}O_2$; EC, ethylene carbonate; EMC, ethyl methylcarbonate; SOC, state-of-charge; P-NCM, pristine $LiNi_{0.5}Co_{0.2}Mn_{0.3}O_2$; C-NCM, surface Co-enriched $LiNi_{0.5}Co_{0.2}Mn_{0.3}O_2$; ICE, initial Coulombic efficiency; CEI, cathode electrolyte interface; PTL, phase transition layer

REFERENCES

(1) Xia, Y.; Zheng, J.; Wang, C.; Gu, M. Designing principle for Ni-rich cathode materials with high energy density for practical applications. *Nano Energy* **2018**, *49*, 434−452.

(2) Martinez, A. C.; Grugeon, S.; Cailleu, D.; Courty, M.; Tran-Van, P.; Delobel, B.; Laruelle, S. High reactivity of the nickel-rich $LiNi_{1-x-y}Mn_xCo_yO_2$ layered materials surface towards H_2O/CO_2 atmosphere and $LiPF_6$-based electrolyte. *J. Power Sources* **2020**, *468*, 228204.

(3) Zhang, S. S. Understanding of performance degradation of $LiNi_{0.80}Co_{0.10}Mn_{0.10}O_2$ cathode material operating at high potentials. *J. Energy Chem.* **2020**, *41*, 135−141.

(4) Kim, U.-H.; Ryu, H. H.; Kim, J. H.; Mücke, R.; Kaghazchi, P.; Yoon, C. S.; Sun, Y. K. Microstructure-Controlled Ni-Rich Cathode Material by Microscale Compositional Partition for Next-Generation Electric Vehicles. *Adv. Energy Mater.* **2019**, *9* (15), 1803902.

(5) Yan, P.; Zheng, J.; Gu, M.; Xiao, J.; Zhang, J. G.; Wang, C. M. Intragranular cracking as a critical barrier for high-voltage usage of layer-structured cathode for lithium-ion batteries. *Nat. Commun.* **2017**, *8*, 14101.

(6) Gent, W. E.; Li, Y.; Ahn, S.; Lim, J.; Liu, Y.; Wise, A. M.; Gopal, C. B.; Mueller, D. N.; Davis, R.; Weker, J. N.; et al. Persistent State-of-Charge Heterogeneity in Relaxed, Partially Charged $Li_{1-x}Ni_{1/3}Co_{1/3}Mn_{1/3}O_2$ Secondary Particles. *Adv. Mater.* **2016**, *28* (31), 6631−6638.

(7) De Jesus, L. R.; Stein, P.; Andrews, J. L.; Luo, Y.; Xu, B.-X.; Banerjee, S. Striping modulations and strain gradients within individual particles of a cathode material upon lithiation. *Mater. Horiz.* **2018**, *5* (3), 486−498.

(8) Ulvestad, A.; Singer, A.; Cho, H. M.; Clark, J. N.; Harder, R.; Maser, J.; Meng, Y. S.; Shpyrko, O. G. Single particle nanomechanics in operando batteries via lensless strain mapping. *Nano Lett.* **2014**, *14* (9), 5123−5127.

(9) Cheng, X.; Zheng, J.; Lu, J.; Li, Y.; Yan, P.; Zhang, Y. Realizing superior cycling stability of Ni-Rich layered cathode by combination of grain boundary engineering and surface coating. *Nano Energy* **2019**, *62*, 30−37.

(10) Xu, X.; Huo, H.; Jian, J.; Wang, L.; Zhu, H.; Xu, S.; He, X.; Yin, G.; Du, C.; Sun, X. Radially Oriented Single-Crystal Primary Nanosheets Enable Ultrahigh Rate and Cycling Properties of $LiNi_{0.8}Co_{0.1}Mn_{0.1}O_2$ Cathode Material for Lithium-Ion Batteries. *Adv. Energy Mater.* **2019**, *9* (15), 1803963.

(11) Su, Y.; Zhang, Q.; Chen, L.; Bao, L.; Lu, Y.; Chen, S.; Wu, F. Stress accumulation in Ni-rich layered oxide cathodes: Origin, impact, and resolution. *J. Energy Chem.* **2022**, *65*, 236−253.

(12) Jiang, M.; Danilov, D. L.; Eichel, R. A.; Notten, P. H. L. A Review of Degradation Mechanisms and Recent Achievements for Ni-Rich Cathode-Based Li-Ion Batteries. *Adv. Energy Mater.* **2021**, *11* (48), 2103005.

(13) Kong, D.; Hu, J.; Chen, Z.; Song, K.; Li, C.; Weng, M.; Li, M.; Wang, R.; Liu, T.; Liu, J.; et al. Ti-Gradient Doping to Stabilize Layered Surface Structure for High Performance High-Ni Oxide Cathode of Li-Ion Battery. *Adv. Energy Mater.* **2019**, *9* (41), 1901756.

(14) Gomez-Martin, A.; Reissig, F.; Frankenstein, L.; Heidbuchel, M.; Winter, M.; Placke, T.; Schmuch, R. Magnesium Substitution in Ni-Rich NMC Layered Cathodes for High-Energy Lithium Ion Batteries. *Adv. Energy Mater.* **2022**, *12* (8), 2103045.

(15) Yang, H. P.; Wu, H. H.; Ge, M. Y.; Li, L. J.; Yuan, Y. F.; Yao, Q.; Chen, J.; Xia, L. F.; Zheng, J. M.; Chen, Z. Y.; et al. Simultaneously Dual Modification of Ni-Rich Layered Oxide Cathode for High-Energy Lithium-Ion Batteries. *Adv. Funct. Mater.* **2019**, *29* (13), 1808825.

(16) Lai, Y.-Q.; Xu, M.; Zhang, Z.-A.; Gao, C.-H.; Wang, P.; Yu, Z.-Y. Optimized structure stability and electrochemical performance of $LiNi_{0.8}Co_{0.15}Al_{0.05}O_2$ by sputtering nanoscale ZnO film. *J. Power Sources* **2016**, *309*, 20−26.

(17) Xu, G.-L.; Liu, Q.; Lau, K. K. S.; Liu, Y.; Liu, X.; Gao, H.; Zhou, X.; Zhuang, M.; Ren, Y.; Li, J.; et al. Building ultraconformal protective layers on both secondary and primary particles of layered lithium transition metal oxide cathodes. *Nat. Energy* **2019**, *4* (6), 484−494.

(18) Qu, X. Y.; Huang, H.; Wan, T.; Hu, L.; Yu, Z. L.; Liu, Y. J.; Dou, A. C.; Zhou, Y.; Su, M. R.; Peng, X. Q.; et al. An integrated surface coating strategy to enhance the electrochemical performance of nickel-rich layered cathodes. *Nano Energy* **2022**, *91*, 106665.

(19) Zhao, C.-Z.; Zhao, Q.; Liu, X.; Zheng, J.; Stalin, S.; Zhang, Q.; Archer, L. A. Rechargeable Lithium Metal Batteries with an In-Built Solid-State Polymer Electrolyte and a High Voltage/Loading Ni-Rich Layered Cathode. *Adv. Mater.* **2020**, *32* (12), 1905629.

(20) Kazzazi, A.; Bresser, D.; Kuenzel, M.; Hekmatfar, M.; Schnaidt, J.; Jusys, Z.; Diemant, T.; Behm, R. J.; Copley, M.; Maranski, K.; et al.

Synergistic electrolyte additives for enhancing the performance of high-voltage lithium-ion cathodes in half-cells and full-cells. *J. Power Sources* **2021**, *482*, 228975.

(21) Zhao, Q.; Wu, Y.; Yang, Z. W.; Song, D. P.; Sun, X. L.; Wang, C.; Yang, L.; Zhang, Y.; Gao, J.; Ohsaka, T.; et al. A fluorinated electrolyte stabilizing high-voltage graphite/NCM811 batteries with an inorganic-rich electrode-electrolyte interface. *Chem. Eng. J.* **2022**, *440*, 135939.

(22) Ryu, H.-H.; Lim, H.-W.; Lee, S. G.; Sun, Y.-K. Near-surface reconstruction in Ni-rich layered cathodes for high-performance lithium-ion batteries. *Nat. Energy* **2024**, *9*, 47−56.

(23) Kim, J.; Ma, H.; Cha, H.; Lee, H.; Sung, J.; Seo, M.; Oh, P.; Park, M.; Cho, J. A highly stabilized nickel-rich cathode material by nanoscale epitaxy control for high-energy lithium-ion batteries. *Energy Environ. Sci.* **2018**, *11* (6), 1449−1459.

(24) Sun, Y. K.; Myung, S. T.; Park, B. C.; Prakash, J.; Belharouak, I.; Amine, K. High-energy cathode material for long-life and safe lithium batteries. *Nat. Mater.* **2009**, *8* (4), 320−324.

(25) Zhao, J.; Zhang, W.; Huq, A.; Misture, S. T.; Zhang, B.; Guo, S.; Wu, L.; Zhu, Y.; Chen, Z.; Amine, K.; et al. In Situ Probing and Synthetic Control of Cationic Ordering in Ni-Rich Layered Oxide Cathodes. *Adv. Energy Mater.* **2016**, *7* (3), 1601266.

(26) Wei, Y.; Zheng, J.; Cui, S.; Song, X.; Su, Y.; Deng, W.; Wu, Z.; Wang, X.; Wang, W.; Rao, M.; et al. Kinetics Tuning of Li-Ion Diffusion in Layered $Li(Ni_xMn_yCo_z)O_2$. *J. Am. Chem. Soc.* **2015**, *137* (26), 8364−8367.

(27) Manthiram, A.; Song, B.; Li, W. A perspective on nickel-rich layered oxide cathodes for lithium-ion batteries. *Energy Storage Mater.* **2017**, *6*, 125−139.

(28) Liu, T.; Yu, L.; Liu, J.; Lu, J.; Bi, X.; Dai, A.; Li, M.; Li, M.; Hu, Z.; Ma, L.; et al. Understanding Co roles towards developing Co-free Ni-rich cathodes for rechargeable batteries. *Nat. Energy* **2021**, *6* (3), 277−286.

(29) Xu, B.; Qian, D.; Wang, Z.; Meng, Y. S. Recent progress in cathode materials research for advanced lithium ion batteries. *Mater. Sci. Eng., R* **2012**, *73* (5−6), 51−65.

(30) Wang, X.; Ding, Y. L.; Deng, Y. P.; Chen, Z. Ni-Rich/Co-Poor Layered Cathode for Automotive Li-Ion Batteries: Promises and Challenges. *Adv. Energy Mater.* **2020**, *10* (12), 1903864.

(31) Huang, W.; Zhao, Q.; Zhang, M.; Xu, S.; Xue, H.; Zhu, C.; Fang, J.; Zhao, W.; Ren, G.; Qin, R.; et al. Surface Design with Cation and Anion Dual Gradient Stabilizes High-Voltage $LiCoO_2$. *Adv. Energy Mater.* **2022**, *12* (20), 2200813.

(32) Li, Z.; Yi, H.; Ren, H.; Fang, J.; Du, Y.; Zhao, W.; Chen, H.; Zhao, Q.; Pan, F. Multiple Surface Optimizations for a Highly Durable $LiCoO_2$ beyond 4.6 V. *Adv. Funct. Mater.* **2023**, *33* (46), 2307913.

(33) Xu, S.; Tan, X.; Ding, W.; Ren, W.; Zhao, Q.; Huang, W.; Liu, J.; Qi, R.; Zhang, Y.; Yang, J.; et al. Promoting Surface Electric Conductivity for High-Rate $LiCoO_2$. *Angew. Chem., Int. Ed. Engl.* **2023**, *62* (10), No. e202218595.

(34) Xie, H.; Peng, H.; Jiang, D.; Xiao, Z.; Liu, X.; Liang, H.; Wu, M.; Liu, D.; Li, Y.; Sun, Y.; et al. Structures, issues, and optimization strategies of Ni-rich and Co-low cathode materials for lithium-ion battery. *Chem. Eng. J.* **2023**, *470*, 144051.

(35) Ding, W.; Ren, H.; Li, Z.; Shang, M.; Song, Y.; Zhao, W.; Chang, L.; Pang, T.; Xu, S.; Yi, H.; et al. Tuning Surface Rock-Salt Layer as Effective O Capture for Enhanced Structure Durability of $LiCoO_2$ at 4.65 V. *Adv. Energy Mater.* **2024**, *14* (13), 2303926.

(36) Li, Z.; Yi, H.; Ding, W.; Ren, H.; Du, Y.; Shang, M.; Zhao, W.; Chen, H.; Zhou, L.; Lin, H.; et al. Revealing the Accelerated Capacity Decay of a High-Voltage $LiCoO_2$ upon Harsh Charging Procedure. *Adv. Funct. Mater.* **2023**, *34* (14), 2312837.

(37) Yi, H.; Du, Y.; Fang, J.; Li, Z.; Ren, H.; Zhao, W.; Chen, H.; Zhou, L.; Zhao, Q.; Pan, F. Revealing the Grain-Boundary-Cracking Induced Capacity Decay of a High-Voltage $LiCoO_2$ at 4.6 V. *ACS Appl. Mater. Interfaces* **2023**, *15* (36), 42667−42675.

(38) Ren, H.; Zhao, W.; Yi, H.; Chen, Z.; Ji, H.; Jun, Q.; Ding, W.; Li, Z.; Shang, M.; Fang, J.; et al. One-Step Sintering Synthesis

Achieving Multiple Structure Modulations for High-Voltage LiCoO$_2$. *Adv. Funct. Mater.* **2023**, *33* (38), 2302622.

(39) Lin, C.; Li, J.; Yin, Z. W.; Huang, W.; Zhao, Q.; Weng, Q.; Liu, Q.; Sun, J.; Chen, G.; Pan, F. Structural Understanding for High-Voltage Stabilization of Lithium Cobalt Oxide. *Adv. Mater.* **2023**, *36* (6), 2307404.

(40) Hu, W.; Peng, Y.; Wei, Y.; Yang, Y. Application of Electrochemical Impedance Spectroscopy to Degradation and Aging Research of Lithium-Ion Batteries. *J. Phys. Chem. C* **2023**, *127* (9), 4465−4495.

(41) Nakayama, M.; Ikuta, H.; Uchimoto, Y.; Wakihara, M. Study on the AC Impedance Spectroscopy for the Li Insertion Reaction of Li$_x$La$_{1/3}$NbO$_3$ at the Electrode−Electrolyte Interface. *J. Phys. Chem. B* **2003**, *107* (38), 10603−10607.

(42) Evans, D. H. Voltammetry: doing chemistry with electrodes. *Acc. Chem. Res.* **1977**, *10* (9), 313−319.

(43) Ulmeanu, S.; Lee, H. J.; Fermin, D. J.; Girault, H. H.; Shao, Y. Voltammetry at a liquid−liquid interface supported on a metallic electrode. *Electrochem. Commun.* **2001**, *3* (5), 219−223.

(44) Homolka, D.; Hung, L. Q.; Hofmanova, A.; Khalil, M. W.; Koryta, J.; Marecek, V.; Samec, Z.; Sen, S. K.; Vanysek, P.; Weber, J.; Brezina, M. Faradaic ion transfer across the interface of two immiscible electrolyte solutions: chronopotentiometry and cyclic voltammetry. *Anal. Chem.* **1980**, *52*, 1606−1610.

(45) Liu, X.; Tan, Y.; Wang, W.; Wei, P.; Seh, Z. W.; Sun, Y. Ultrafine Sodium Sulfide Clusters Confined in Carbon Nano-polyhedrons as High-Efficiency Presodiation Reagents for Sodium-Ion Batteries. *ACS Appl. Mater. Interfaces* **2021**, *13* (23), 27057−27065.

(46) Moškon, J.; Gaberšček, M. Transmission line models for evaluation of impedance response of insertion battery electrodes and cells. *J. Power Sources Adv.* **2021**, *7*, 100047.

(47) Zhang, B.; Wang, L.; Zhang, Y.; Wang, X.; Qiao, Y.; Sun, S.-G. Reliable impedance analysis of Li-ion battery half-cell by standardization on electrochemical impedance spectroscopy (EIS). *J. Chem. Phys.* **2023**, *158* (5), 054202.

(48) Kühn, S. P.; Edström, K.; Winter, M.; Cekic-Laskovic, I. Face to Face at the Cathode Electrolyte Interphase: From Interface Features to Interphase Formation and Dynamics. *Adv. Mater. Interfaces* **2022**, *9* (8), 2102078.

(49) Wang, W.; Yang, Q.; Qian, K.; Li, B. Impact of evolution of cathode electrolyte interface of Li(Ni$_{0.8}$Co$_{0.1}$Mn$_{0.1}$)O$_2$ on electrochemical performance during high voltage cycling process. *J. Energy Chem.* **2020**, *47*, 72−78.

(50) Huang, W.; Lin, C.; Zhang, M.; Li, S.; Chen, Z.; Zhao, W.; Zhu, C.; Zhao, Q.; Chen, H.; Pan, F. Revealing Roles of Co and Ni in Mn-Rich Layered Cathodes. *Adv. Energy Mater.* **2021**, *11* (41), 2102646.

(51) Zhang, S. S. Problems and their origins of Ni-rich layered oxide cathode materials. *Energy Storage Mater.* **2020**, *24*, 247−254.

(52) Ryu, H.-H.; Namkoong, B.; Kim, J.-H.; Belharouak, I.; Yoon, C. S.; Sun, Y.-K. Capacity Fading Mechanisms in Ni-Rich Single-Crystal NCM Cathodes. *ACS Energy Lett.* **2021**, *6* (8), 2726−2734.

(53) Liu, P.; Yang, L.; Xiao, B.; Wang, H.; Li, L.; Ye, S.; Li, Y.; Ren, X.; Ouyang, X.; Hu, J.; et al. Revealing Lithium Battery Gas Generation for Safer Practical Applications. *Adv. Funct. Mater.* **2022**, *32* (47), 2208586.

(54) Zhao, H.; Wang, J.; Shao, H.; Xu, K.; Deng, Y. Gas Generation Mechanism in Li-Metal Batteries. *Energy Environ. Mater.* **2022**, *5* (1), 327−336.

(55) Lu, Y.-C.; Mansour, A. N.; Yabuuchi, N.; Shao-Horn, Y. Probing the Origin of Enhanced Stability of "AlPO$_4$" Nanoparticle Coated LiCoO$_2$ during Cycling to High Voltages: Combined XRD and XPS Studies. *Chem. Mater.* **2009**, *21* (19), 4408−4424.